Mesoscale Reaction–Diffusion Phenomena Governing Lignin-First Biomass Fractionation

Nicholas E. Thornburg,[a] M. Brennan Pecha,[b] David G. Brandner,[a] Michelle L. Reed,[b] Josh V. Vermaas,[b] William E. Michener,[b] Rui Katahira,[a] Todd B. Vinzant,[b] Thomas D. Foust,[a] Bryon S. Donohoe,[b] Yuriy Román-Leshkov,[c] Peter N. Ciesielski,*[b] and Gregg T. Beckham*[a]

Lignin solvolysis from the plant cell wall is the critical first step in lignin depolymerization processes involving whole biomass feedstocks. However, little is known about the coupled reaction kinetics and transport phenomena that govern the effective rates of lignin extraction. Here, we report a validated simulation framework that determines intrinsic, transport-independent kinetic parameters for the solvolysis of lignin, hemicellulose, and cellulose upon incorporation of feedstock characteristics for the methanol-based extraction of poplar as an example fractionation process. Lignin fragment diffusion is predicted to compete on the same time and length scales as reactions of lignin within cell walls and longitudinal pores of typical milled particle sizes, and mass transfer resistances are predicted to dominate the solvolysis of poplar particles that exceed approximately 2 mm in length. Beyond the approximately 2 mm threshold, effectiveness factors are predicted to be below 0.25, which implies that pore diffusion resistances may attenuate observable kinetic rate measurements by at least 75% in such cases. Thus, researchers are recommended to conduct kinetic evaluations of lignin-first catalysts using biomass particles smaller than approximately 0.2 mm in length to avoid feedstock-specific mass transfer limitations in lignin conversion studies. Overall, this work highlights opportunities to improve lignin solvolysis by genetic engineering and provides actionable kinetic information to guide the design and scale-up of emerging biorefinery strategies.

Introduction

Lignin is an abundant, aromatic macromolecule that comprises 15–25 wt% of lignocellulosic biomass.[1] Aside from traditional pulping processes[2] that are destructive to native lignin,[3] myriad techniques have been studied for lignin removal, such as organosolv fractionation,[4] alkaline pretreatment,[5] ionic liquid pretreatment,[6] and others,[7] with predominant emphasis on the improvement of polysaccharide accessibility for depolymerization and upgrading.[8] Beyond biomass conversion, delignification is also important for emerging biomaterial applications that seek to modify various physicochemical properties of wood.[9]

Reductive catalytic fractionation (RCF) is a historical technique[10] that has recently garnered renewed attention[1a,11] from lignin valorization researchers because of its attractive features of high-yield catalytic chemistries that lead to a narrow slate of *n*-propyl- and *n*-propanol-functionalized methoxyphenols.[1a] RCF is an active stabilization technique that employs tandem solvolysis (i.e., solvent-mediated extraction) of covalently bound and/or physisorbed lignin from the cell wall, followed by hydrogenolysis, hydrogenation, and hydrodeoxygenation reactions facilitated by a heterogeneous reduction catalyst.[12] Hardwoods are commonly reported to be advantageous substrates for RCF because of their high ether bond content, which leads to higher yields of monomeric products compared to that obtained from softwoods and herbaceous feedstocks.[1a,c]

The majority of reports on RCF describe batch reactor studies, in which the biomass and catalyst are intermixed.[1a] Catalyst composition and performance are often emphasized, whereas investigation of the solvolysis step in isolation is also important.[13] Previously, we hypothesized that lignin solvolysis is limited by mass transport during batch-mode RCF because of apparent differences in productivity and calculated activation energy if the poplar particle size was varied.[13a] Early work

[a] Dr. N. E. Thornburg, D. G. Brandner, Dr. R. Katahira, Dr. T. D. Foust, Dr. G. T. Beckham
National Bioenergy Center
National Renewable Energy Laboratory
15013 Denver West Parkway, Golden, CO 80401 (USA)
E-mail: Gregg.Beckham@nrel.gov

[b] Dr. M. B. Pecha, M. L. Reed, Dr. J. V. Vermaas, W. E. Michener, T. B. Vinzant, Dr. B. S. Donohoe, Dr. P. N. Ciesielski
Biosciences Center
National Renewable Energy Laboratory
15013 Denver West Parkway, Golden, CO 80401 (USA)
E-mail: Peter.Ciesielski@nrel.gov

[c] Prof. Y. Román-Leshkov
Department of Chemical Engineering
Massachusetts Institute of Technology
77 Massachusetts Avenue, Cambridge, MA 02139 (USA)

Supporting Information and the ORCID identification number(s) for the author(s) of this article can be found under: https://doi.org/10.1002/cssc.202000558.

This publication is part of a Special Issue focusing on "Lignin Valorization: From Theory to Practice". Please visit the issue at http://doi.org/10.1002/cssc.v13.17

by Saka et al. highlighted broad performance trends in lignin methanolysis,[14] though particle size effects and mass and heat transfer were not considered alongside primary solvolytic chemical reactions. Aside from these works, few studies have been attempted to understand the chemical kinetics that underlie solvolysis treatments.[13a,15]

Unlike the pulp and paper industry, which relies on complex transport models[16] to optimize lignin extraction during processing, catalytic lignin upgrading efforts to date seldom consider coupled reaction–diffusion models. This is needed, however, given the complex natural pore structures, varying tissue morphologies,[17] and diverse particle sizes and aspect ratios,[18] which is illustrated in Figure 1 for a typical poplar substrate. Indeed, decoupling intrinsic reaction and transport phenomena is indispensable to optimize reactor performance for lignin valorization processes that utilize a variety of biomass feedstocks.

In this work, we present a generalizable approach to determine the intrinsic kinetics of solvent-based fractionation, using poplar methanolysis as a test case. Internal and external features of milled poplar are measured directly by fluorescence microscopy and optical particle size analysis, respectively. These geometric descriptors enable the construction of a family of realistic, 3D particle models with a feedstock-specific microstructure by using previously established algorithms,[18b] as well as simplified, 2D[20] particle models of reduced order. The latter are used to fit non-isothermal kinetic parameters for lignin, hemicellulose, and cellulose extractions from a representative particle size range by using time–course solids compositional data following methanol treatment and approximations of the diffusion of each species from molecular dynamics (MD) simulations. Intrinsic rate constants are then extended to other particle sizes and to the 3D models to demonstrate the bulk feedstock behavior and to estimate the impacts of mass transfer resistances that occur during solvolysis. Mesoscale mass transfer limitations are predicted to pose severe consequences for practical lignin valorization systems, which illustrates the importance of decoupling transport phenomena from chemical kinetics for lignin-first process optimization.

Results

Poplar sieve fractionation and experimental design

A primary objective of this study is to understand the decoupled effects of reaction temperature, residence time, and poplar particle size in lignin-first fractionation by methanol. To assess the role of particle size, 53.5 g of milled extractives-free hybrid poplar were fractionated into five nominal ranges: >1000, 500–1000, 250–500, 125–250, and <125 μm. A Gaussian-like distribution was observed among the five ranges (Figure S1). The 250–500 μm range comprised 53.1 wt%, which suggests that it is largely representative of the parent feedstock. Batch reactions were performed in sealed vessels that contained only methanol (12.00 mL) and biomass (0.500 g) heated rapidly inside a fluidized sand bath (see Supporting Information for methods). Nearly identical time–course solid extraction profiles were observed for the 250–500 μm range and the bulk material at 220 and 250 °C, and triplicate extractions of the sieved material at 250 °C after 10.0 min exhibited <4% standard deviation (Figure S2). Therefore, as an important simplification for particle modeling, we may make practical inferences about the bulk feedstock based on the reproducible, mirrored performance of its dominant fraction.

In general, the proper assessment of diffusion in reactive processes requires the decoupling of other bulk mass transfer effects, such as advection (i.e., fluid flow).[21] Hence, in all kinetic experiments reported here, no external or internal agitation is applied to batch reactors. The vessels are sufficiently heavy to resist agitation by the fluidized sand bath heating medium, which itself affords the ability to rapidly heat reactors at timescales relevant to reaction–diffusion studies; indeed, heat-up periods on the order of ≤ 5 min were observed for a given temperature (Figure S3). Thus, although natural convection may induce some minor fluid movement, diffusion is considered to be the primary mode of mass transfer, driven by concentration gradients that arise from methanol extraction events. Further, owing to the complex compositions of liquid solvolysis products[22] that make quantitative analytics challenging,[3,23] here we traced changes in solid compositions by

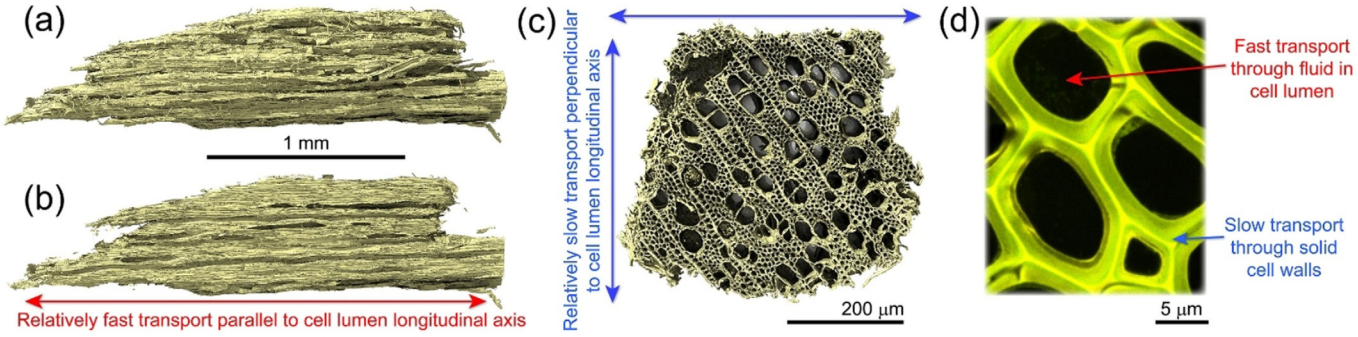

Figure 1. Visualization of the structure of a milled poplar wood particle and its modes of internal mass transport. a) Full X-ray computed tomography (XCT) reconstruction[19] of a poplar particle. b) Longitudinal XCT cross-section, which illustrates high-aspect ratio cell lumen (pores) aligned with the major axis of the particle. c) Transverse XCT cross-section, which illustrates the distribution of vessel elements (large pores) and fiber cells (small pores). d) Optical micrograph of fiber cells in a transverse cross-section.

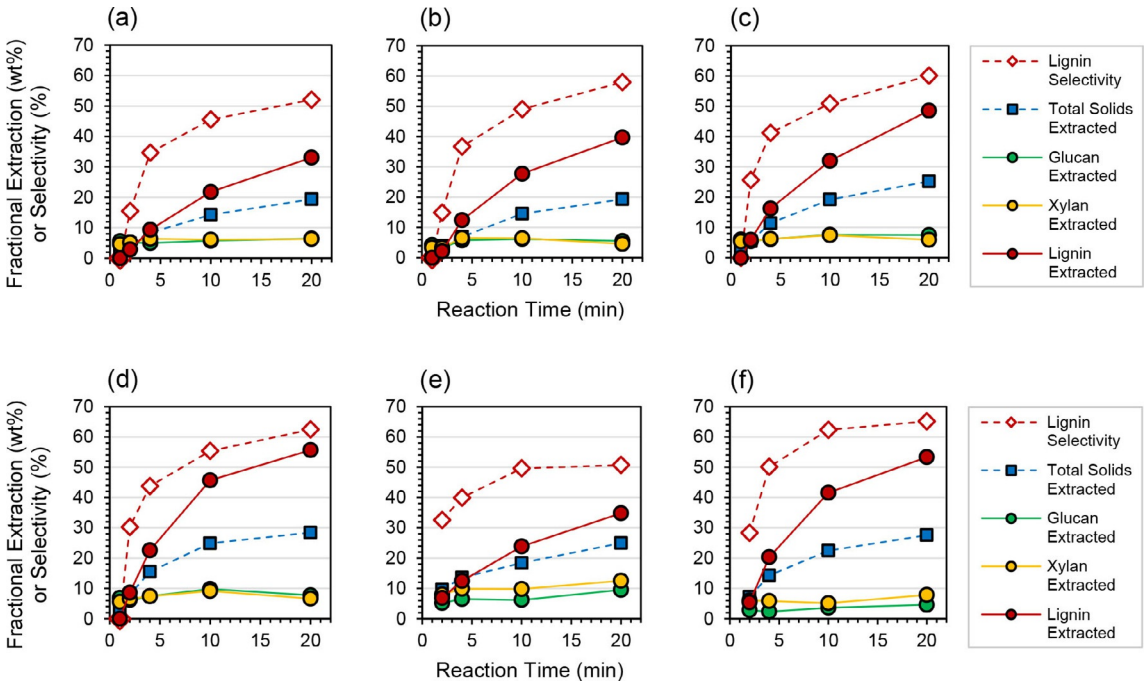

Figure 2. Time–course profiles of fractional[a] and total[b] extractions and of lignin selectivity[c] for methanol extraction of poplar under various conditions: a) 250–500 μm at 220 °C (41 bar), b) 250–500 μm at 230 °C (89 bar), c) 250–500 μm at 240 °C (136 bar), d) 250–500 μm at 250 °C (183 bar), e) < 125 μm at 220 °C (41 bar), and f) 500–1000 μm at 250 °C (183 bar). Connecting lines drawn for clarity. All extraction values correspond to changes in dry poplar pulp composition as a result of treatment. [a] Fractional extraction [wt%] at time t = [1 − (mass final component)/(mass initial component)] × 100. [b] Total solids extracted [wt%] at time t = [1 − (mass final poplar)/(mass initial poplar)] × 100. [c] Lignin selectivity [%] at time t = (mass lignin extracted)/(mass total components extracted) × 100.

using standard compositional analysis protocols[24] for pre- and post-reaction poplar samples. To simplify the systems of kinetic equations in finite element method-based computational fluid dynamics (CFD) models, time–course fractional extraction profiles were only traced for the three major cell wall components: lignin, hemicellulose, and cellulose. The fresh, bulk feedstock and the four primary sieve fractions overall share nearly identical compositions (Table S1). These similarities imply that physical size reductions do not change cell wall compositions, which enables the determination of intrinsic kinetics among this suite of milled particle fractions.

Empirical performance trends in poplar methanolysis

Batch solvolysis reactions were performed using the 250–500 μm poplar fraction at 220–250 °C under autogenous pressure with residence times of 1.0–20.0 min. Fractional extraction profiles of lignin, xylan, and glucan are shown in Figure 2 a–d alongside the total solids extracted (i.e., converted) and the selectivity to lignin. As expected, apparent rates of extraction increase with the increasing temperature, most notably for lignin species. Uniquely, carbohydrate fragments are extracted to their maximum extents (< 10 wt%) within 1.0 min of the initiation of heating, which implies low activation barriers for these reactions. The influence of particle size is considered briefly for two extremes: (i) < 125 μm at 220 °C and (ii) 500–1000 μm at 250 °C (Figure 2 e–f). Compared with the 250–500 μm range at each temperature, apparent rates of lignin extraction and of total solids extraction increase modestly with the decrease of the particle size, consistent with a non-negligible role of intraparticle mass transport. In contrast, the xylan and glucan extraction profiles again remain flat after short residence times, seemingly unaffected by particle size.

Broad trends in lignin selectivity as a function of extraction are observed across the entire kinetic data set. Selectivity to lignin extraction increases monotonically with total extraction extent and collapses along a single trend across all conditions and poplar particle sizes (Figure 3 a). Practically, only lignin species appear to be extracted from poplar after approximately 2 min residence time in all reactors. Further, for a given extent of total solids extraction, all lignin selectivities vary within approximately 10–12% of one another. At approximately 15 wt% isoextraction (Figure 3 a, inset circle), the lignin molecular weight (MW) distributions obtained by using gel permeation chromatography (GPC) are virtually identical (Figure 3 b). Finally, carbohydrate retentions in post-reaction pulps are > 89 wt% across every experiment (Figure 3 c). Taken together, these trends suggest that the same chemistry is happening within each particle, despite their differences in size.

However, despite the uniformity among broad trends in selectivity as a function of extraction, true kinetic parameters cannot be determined solely from the time–course profiles illustrated in Figure 2. In part, this is limited by the rapid, single-minute timescales of methanol extractions that occur during reactor heat-up (Figure S3). Furthermore, the modest, non-negligible differences in apparent reactivities across different particle sizes suggests an influence of intraparticle mass transfer. Thus, we must account for both non-isothermality and trans-

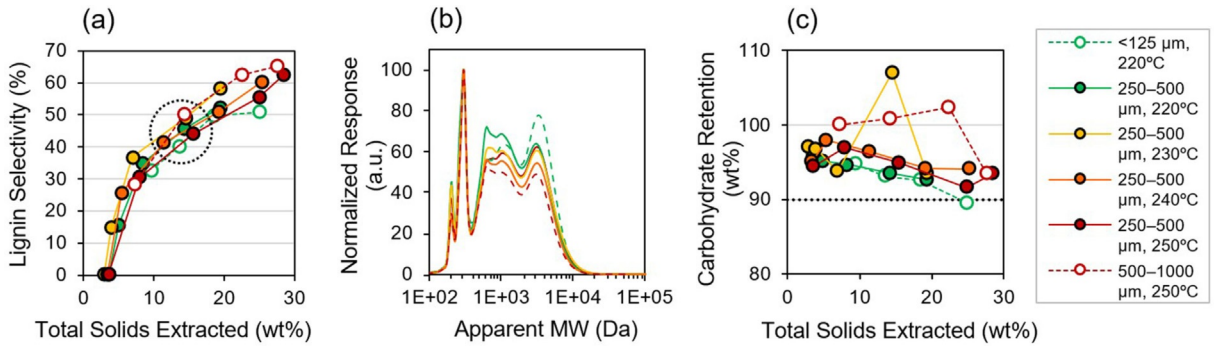

Figure 3. Empirical performance trends in methanol extraction of poplar: a) lignin selectivity as a function of extent of total solids extraction (connecting lines drawn for clarity; inset circle illustrates ≈15 wt% isoextraction data subset), b) GPC lignin MW distributions at approximately 15 wt% isoextraction, and c) carbohydrate retentions[a] as a function of total solids extracted (connecting lines drawn for clarity; dotted black line illustrates 90 wt% line). [a] Carbohydrate retention [wt%] = (mass final carbohydrate)/(mass initial carbohydrate) × 100, in which carbohydrate = [glucan+xylan+galactan+arabinan+mannan].

port phenomena before we attempt to extract intrinsic kinetic information from these data, and we used the 250–500 µm fraction as a basis for reaction–diffusion model development.

Construction of poplar particle models

Milled poplar contains a wide spectrum of nominal particle size ranges (Figure S1), and each range exhibits significant variability within its particle population and even within the internal tissue microstructure of each particle (Figure 1). To understand these differences, optical descriptors of morphological attributes (e.g., Feret measurements) were collected for the bulk feedstock and for its four major sieve fractions (Figure S4), and various transverse cell wall and lumen (i.e., pore) features were quantified by using confocal scanning laser microscopy (CSLM; Figure S5).[25] The resulting measurements are statistically meaningful (Figures S6–S7, Table S2) and are presented in Tables 1 and 2.

Four key observations are made. First, Feret width or thickness values of sieved samples closely resemble the lower limit of the nominal size range for each fraction (Table 1), which implies that these rod-like particles readily pass through square-shaped mesh openings.[18a] Thus, sieving discriminates particles predominantly by their thinner dimensions. Second, the bulk feedstock displays intermediate values in close agreement with the measurements of the 250–500 µm fraction (Table 1), which further corroborates the choice of this fraction as the basis for subsequent model development. Third, significant variability is noted in cell wall thicknesses and in lumen size distributions (Table 2), particularly among fiber cells, the most abundant cell type seen in transverse sections (Figure 1c and Figure S5a). Fourth, lignin is most notably localized in the compound middle lamella (i.e., the bright orange signatures of Figure S5b and c), consistent with visualizations by others.[26] From a mass transfer perspective, lignin fragments solvolytically cleaved and/or liberated by methanol must diffuse through the cell wall before they enter the lumen for transport out of the particle.

Next, 3D particle models that correspond to the four main poplar sieve fractions were constructed from the geometric descriptors given in Tables 1 and 2. The generalizable algorithms that underlie these constructions were described previously.[18b] The final 3D models (Figure 4) are readily implemented into the CFD solver COMSOL Multiphysics.

As kinetic parameter extraction requires us to perform multiple iterative simulations within a parameter optimization routine, reduced-order models[20] (ROMs) were developed to accelerate multiparametric kinetic data fitting and broader sensitivity analysis. In contrast to 3D particle models, ROM geometries omit explicit microstructural features and assume an average

Table 1. Summary of mean external particle geometries for various poplar fractions.

Poplar fraction [µm]	L_F[a] [µm]	W_F or d_F[a] [µm]	L_F/W_F or L_F/d_F
<125	138 ± 27.4	54.4 ± 23.1	2.54
125–250	369 ± 70.7	139 ± 53.1	2.66
250–500[b]	1103 ± 153	274 ± 135	4.02
500–1000[b]	1488 ± 231	474 ± 196	3.14
bulk feedstock	910 ± 178	249 ± 126	3.65

[a] L_F = Feret length; secondary values represent single standard deviations from the mean. Feret width (W_F) or thickness (d_F) represent thinner dimensions measured from the 2D particle size analysis. See Figure S4. [b] For these fractions, a volume-weighted average was computed from the two largest volumetric bins to determine reported dimensions. See Figure S6b and c.

Table 2. Mean microstructure dimensions calculated from CSLM micrographs.

Parameter	Mean measurement[a]
Fiber cell wall thickness [µm]	2.1 ± 0.6
Fiber cell lumen area [µm^2]	68.9 ± 51.3
Fiber cell lumen circular diameter [µm]	8.2 ± 4.4
Vessel cell lumen area [µm^2]	1790 ± 401
Vessel cell lumen circular diameter [µm]	47.8 ± 5.2
Spatial frequency of vessel cells [mm^{-2}]	150 ± 26
Ray cell spacing[b] [µm]	83.1 ± 27.4
Average void fraction[c]	0.587

[a] Secondary values represent single standard deviations from the mean. See Figures S5 and S7 and Table S2 for measurements and regions of interest used. [b] Ray cell spacing provides information about the periodicity of vessel cell growth. See Figure S5a. [c] Calculated from globally averaged ratios of summed lumen areas to total cross-sectional area within each region of interest. See Table S2.

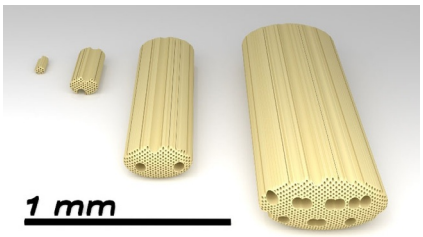

Figure 4. Orthographic visualization of 3D particle models with realistic morphologies and resolved microstructures, representative of the four major poplar sieve fractions.

uniform porosity as per Darcy's Law. Specifically, the poplar void fraction is determined from existing micrograph measurements by using cross-sectional area ratio calculations (Table 2, final entry). Upon the averaging of the width and thickness semiaxes, models can be further reduced to two dimensions, which incorporate axisymmetry along the long axis of the particle with an additional symmetry plane through its short axis (Figure 5). This dimensional reduction results in 2D particles with integrated volume and surface area values with $\geq$95% agreement to those of 3D particles. Finally, the introduction of a methanol solution domain with no-flux at the exterior edges (i.e., top and right boundaries in Figure 5) and finite element meshing completes the preparation of the simulation space for CFD modeling.

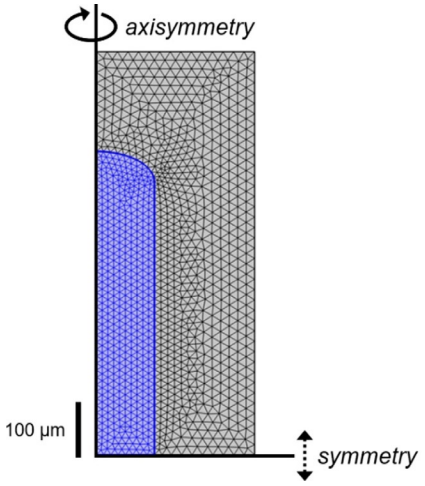

Figure 5. 2D axisymmetric ROM mesh of a representative 250–500 µm particle (blue) and surrounding methanol domain (gray). The left boundary obeys axisymmetry, whereas the bottom boundary obeys symmetry; top and right methanol domain boundaries obey no-flux conditions. Model geometry and mesh generated by using COMSOL Multiphysics 5.4.

Reaction–diffusion model development in two dimensions

A goal of this investigation is to capture non-isothermal kinetic behaviors of lignin, hemicellulose, and cellulose extractions from poplar particles of various sizes with the incorporation of simultaneous mass transfer. The non-isothermality of the system was described by explicit temperature profiles [Eqs. (S2) and (S3)] characteristic of the reactor heat-up period, in which setpoints are reached typically within 4–5 min of heating (Figure S3). Kinetic rate constants and diffusion coefficients are necessarily temperature-dependent functions, so the prescription of a global, residence-time-dependent temperature profile obviates the need to assume models of mesoscale heat transfer behavior.

Accordingly, the decoupling of intrinsic kinetics from diffusion requires assumptions about molecular mass transfer within both the free solution and cell wall domains. Although the measurement of diffusion coefficients within biomass is challenging under experimentally relevant conditions,[27] fluid diffusion coefficients may instead be computed readily by using MD simulations upon defining representative solute species and solvation environments. Lignin MW distributions obtained by using GPC are invariant at an intermediate extent of isoextraction (Figure 3b). Complementary GPC analysis of time-course oil samples from the extraction of the 250–500 µm fraction at 250 °C reveals a similar invariance, and the number-average MWs vary between 550 and 800 Da consistent with tetrameric lignin species (Table S3). Carbohydrate products, extracted from product oils by using water/dichloromethane, were characterized by using liquid chromatography to identify oligomers of relative abundance; this qualitative analysis reveals a pentose series of repeat units of *m/z* 132 that spans a degree of polymerization (DP) of 1–10 and a hexose series of repeat units of *m/z* 162 that spans a DP of 1–6.

Molecular diffusion coefficients and their temperature dependence over 25–250 °C have been calculated for lignin,[28] xylan,[29] and glucan[29] fragments solvated in methanol[30] by using MD simulations[31] alongside the corresponding methanol self-diffusion coefficients [see Eq. (S1)]. The resulting coefficient sets for select species were fitted empirically to exponential functions of absolute temperature (Figure S8) for use as model inputs. Relationships among the lignin diffusion coefficients ($D_{F,lig}$) as a function of solute MW are illustrated in Figure 6. Briefly, $D_{F,lig}$ values are reasonably sensitive to temperature but less sensitive to lignin chain length, and typically vary within the same order of magnitude across DP = 1–20.

Thus, for base-case models, tetramer species are assumed as mid-range input MWs for each of the three cell wall components, with dimers and decamers considered as sensitivity cases. Although apparent MWs up to approximately 10000 Da are observed in product oils (Figure 3b), decameric solutes (1992 Da) are the largest lignin species considered to have originated from the plant cell wall.[32] Lastly, the dependence of diffusion coefficients on the autogenous system pressure was not considered, given the weak influence of pressure on molecular diffusivities.

Having defined fluid diffusion coefficients $D_{F,i}$, solute effective diffusivities $D_{e,i}$ [Eq. (1)] within 2D axisymmetric particle pores may be calculated from the average void fraction ε_P of the feedstock (initial value for fresh poplar listed in Table 2) and an assumed model of tortuosity[33] τ [Eq. (2)]:

$$D_{e,i} = \frac{\varepsilon_P}{\tau} D_{F,i}, \text{ where} \quad (1)$$

$$\tau = \varepsilon_P^{-1/3} \quad (2)$$

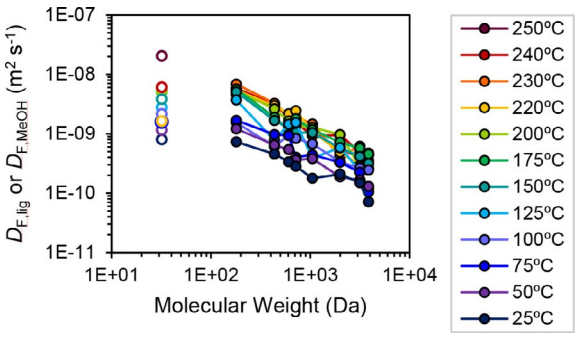

Figure 6. Fluid diffusion coefficients of lignin (connected solid data points, right) and methanol (isolated open data points, left) solvated in methanol as a function of solute molecular weight at 25–250 °C estimated by MD simulations.

Given the preponderance of longitudinal pore structures in woody plants (Figure 1 and Figure S5), axial diffusion is favored heavily, by up to four orders of magnitude relative to radial diffusion in some cases.[34] For ROMs, an anisotropic retardation factor of 10^{-2} is prescribed along the radial dimension in pore diffusivity tensors. Notably, the particle void fraction ε_P necessarily changes as a function of residence time t because of the conservation of volume (and thus, the conservation of mass in a constant density system); this quantity is rendered as a function of the change of component mass fractions, scaled to the extent of extraction, and generally ranges from 0.587 to 0.653. Lastly, Darcy's law and Fick's second law [Eq. (3)] were assumed to describe diffusion and reaction (R_i) within uniformly distributed particle pores for each of three species i of concentrations [i], whereas the mass continuity equation [Eq. (4)] was assumed to describe reaction and diffusion in the solution phase:

$$\frac{\partial(\varepsilon_P[\mathrm{i}])}{\partial t} + \nabla \cdot \left(-D_{\mathrm{e,i}} \nabla[\mathrm{i}]\right) = R_{\mathrm{i}} \tag{3}$$

$$\frac{\partial[\mathrm{i}]}{\partial t} + \nabla \cdot \left(-D_{\mathrm{F,i}} \nabla[\mathrm{i}]\right) = R_{\mathrm{i}} \tag{4}$$

Next, a suitable reaction network must be chosen to describe the kinetics of lignin, xylan, and glucan reactive extractions by methanol. For the carbohydrates, the time–course reaction profiles shown in Figure 2 highlight equilibrium-like behavior, in which maximum extents of extraction are achieved and remain unchanged after early residence times. Profiles of this kind are described readily by quasi-equilibrium rate laws of pseudo-first order in each species. Conceptually, such rate laws describe an extraction event that involves methanol and intact carbohydrate (i.e., the forward reaction) followed by a redeposition event (i.e., the reverse reaction), in which a xylan or glucan fragment may redeposit within the cell wall or on the lumen surface.[35] An analogous scheme was assigned for lignin extraction and redeposition, given its well-known tendency to redeposit within biomass pores through physical[35,36] and chemical[1a,35,37] condensation. This phenomenon was observed directly on spent poplar tissues (Figure S9). A general reversible consumption rate law ($-R_i$) for pseudo-second-order extraction (forward reaction, f) followed by pseudo-first-order redeposition (reverse reaction, r) is described in Equation (5), in which the species i is lignin, xylan, or glucan, and subscripts P and S denote particle and solution domains, respectively:

$$-R_{\mathrm{i}} = k_{0,\mathrm{i,f}} e^{-E_{\mathrm{a,i,f}}/RT} [\mathrm{i}]_{\mathrm{P}} [\mathrm{MeOH}] - k_{0,\mathrm{i,r}} e^{-E_{\mathrm{a,i,r}}/RT} [\mathrm{i}]_{\mathrm{S}} \tag{5}$$

We note that other rate laws, such as irreversible extractions [i.e., forward reaction only from Eq. (5)] and/or those with varied integer reaction orders, did not provide adequate data fits.

Kinetic parameter determination

The pre-exponential factors $k_{0,i,f}$ and $k_{0,i,r}$ and activation barriers $E_{a,i,f}$ and $E_{a,i,r}$ in Equation (5) were fitted systematically to the experimental data from Figure 2 a–d in MATLAB by using iterative COMSOL calculations (see Supporting Information for methodology). Rate constants were fitted for cases of lignin dimer species (436 Da), lignin tetramers (715 Da; base case), and lignin decamers (1992 Da), each with a unique diffusion coefficient temperature profile (Figure 6 and Figure S8) input into the mass transfer model. Mean values and standard deviations across 10 independent fitting rounds for each of these cases are summarized in Table 3. Small standard deviations of 1–18% are observed, which highlights the robustness of the fitting strategy. Good agreement is observed across the different MW cases. Notably, minor differences are observed in lignin extraction pre-exponential factors ($k_{0,lig,f}$), a parameter that may compensate mathematically for differences in the diffusion resistance of a given species; indeed, $k_{lig,f}$ trends inversely with $D_{F,lig}$ for the size of each species at each reaction temperature (Figure S10). Lastly, we note that k_0 and E_a values are only valid if taken as quartets for each reactive species.

For a given lignin oligomer size, significant differences are observed among the three reactive species in magnitudes of both pre-exponential factors and activation barriers. For carbohydrates, low barriers of approximately 30–40 kJ mol^{-1} are determined for each reaction direction in Equation (5), whereas redeposition rate coefficients are approximately 1–2 orders of magnitude larger than those of lignin redeposition. Conceptually, these findings are consistent with rapid carbohydrate extractions that reach quasi-equilibrated extents at subfinal temperatures within minutes of the start of reaction. Lignin extraction accordingly exhibits a higher barrier of approximately 58 kJ mol^{-1}, requiring higher temperatures and hence longer residence times. Values of $E_{a,lig,f}$ are also in agreement with apparent barriers reported elsewhere,[13a,15a] although without the decoupling of mesoscale mass transfer and non-isothermality.

Mean best-fit rate constants from the tetramer base case given in Table 3 were used to simulate three-component extraction from a 250–500 μm particle at 220–250 °C. Model profiles are illustrated in Figure S11 and generally exhibit excellent agreement with experimental data. Some overprediction is noted at lower temperatures (Figure S11 a and b), though closer agreement with data is observed at 240 and 250 °C (Figure S11 c and d). Overall, 2D ROM best-fits yield excellent rep-

Table 3. Mean kinetic parameters and standard deviations that result from 10 independent trails[a] of fitting 250–500 μm fractional extraction data collected at 220–250 °C.

Species	Kinetic parameter[a]	Assumed lignin speciation[b] dimer[a,c] (436 Da)	tetramer[a,c,d] (715 Da)	decamer[a,c] (1992 Da)
lignin	$k_{0,lig,f}$ [$m^3\,mol^{-1}\,s^{-1}$]	$6.11\times10^{-2}\pm8.41\times10^{-3}$	$5.79\times10^{-2}\pm8.28\times10^{-3}$	$5.28\times10^{-2}\pm6.84\times10^{-3}$
	$E_{a,lig,f}$ [$kJ\,mol^{-1}$]	58.8 ± 0.57	58.5 ± 0.82	57.0 ± 1.52
	$k_{0,lig,r}$ [s^{-1}]	$1.93\times10^{3}\pm2.53\times10^{2}$	$1.78\times10^{3}\pm1.45\times10^{2}$	$1.97\times10^{3}\pm2.55\times10^{2}$
	$E_{a,lig,r}$ [$kJ\,mol^{-1}$]	52.4 ± 1.96	52.5 ± 2.14	52.4 ± 3.27
xylan	$k_{0,xyl,f}$ [$m^3\,mol^{-1}\,s^{-1}$]	$3.37\times10^{-3}\pm4.57\times10^{-4}$	$3.19\times10^{-3}\pm4.85\times10^{-4}$	$3.28\times10^{-3}\pm4.75\times10^{-4}$
	$E_{a,xyl,f}$ [$kJ\,mol^{-1}$]	31.1 ± 3.46	30.9 ± 3.25	31.4 ± 3.42
	$k_{0,xyl,r}$ [s^{-1}]	$9.33\times10^{3}\pm1.12\times10^{3}$	$9.40\times10^{3}\pm1.01\times10^{3}$	$9.60\times10^{3}\pm1.19\times10^{3}$
	$E_{a,xyl,r}$ [$kJ\,mol^{-1}$]	31.2 ± 3.91	31.2 ± 3.95	30.8 ± 3.23
glucan	$k_{0,glc,f}$ [$m^3\,mol^{-1}\,s^{-1}$]	$3.88\times10^{-2}\pm3.74\times10^{-3}$	$4.20\times10^{-2}\pm6.31\times10^{-3}$	$4.03\times10^{-2}\pm7.34\times10^{-3}$
	$E_{a,glc,f}$ [$kJ\,mol^{-1}$]	38.9 ± 3.81	39.8 ± 4.05	38.8 ± 3.73
	$k_{0,glc,r}$ [s^{-1}]	$9.88\times10^{4}\pm1.28\times10^{4}$	$9.17\times10^{4}\pm1.53\times10^{4}$	$9.66\times10^{4}\pm1.68\times10^{4}$
	$E_{a,glc,r}$ [$kJ\,mol^{-1}$]	38.7 ± 3.50	39.2 ± 3.65	38.5 ± 3.87

[a] Equation (5) parameter values represent local solutions that result from the averaging of 10 trials using initial guesses of ±20% random perturbation. See Supporting Information for details. [b] Lignin speciation determines both input molecular weight and the associated temperature-dependent diffusion profile (Figure 6 and Figure S8) used in models. The former affects absolute values of $k_{0,lig,f}$ and $k_{0,lig,r}$ (caused by different starting moles of lignin), whereas the latter influences diffusion resistances independent of the chemistry. [c] Secondary values represent single standard deviations from the mean. [d] Mean kinetic parameters determined from this scenario are subsequently referred to and utilized as the "base case" in this report.

resentations of actual extraction behavior, as depicted in the parity plot shown in Figure S11 e.

Numerous sensitivity analyses were performed across various limiting cases of kinetic and mass transfer parameters, which are all shown to be largely insensitive to model outputs. Detailed results are discussed in the Supporting Information and summarized in Table S4 and Figures S12–S17.

Ensemble calculations using 2 D axisymmetric models

Overall, 2 D axisymmetric reaction–diffusion models for lignin, hemicellulose, and cellulose extractions from a representative 250–500 μm poplar particle are robust, which warrants validation with other particle sizes to enable the prediction of bulk feedstock behavior under similar extraction conditions. First, base-case predictive simulations were performed for a representative <125 μm particle at 220 °C to benchmark against fractional extraction data from Figure 2 e; analogous simulations were also performed for a representative 500–1000 μm particle at 250 °C for comparison with Figure 2 f. Results are illustrated in Figure S18. Our 2 D model predictions for these small and large particle sizes generally show excellent agreement with the data; minor overprediction is noted in <125 μm simulations at longer residence times, although with similarly small variance as in best-fit simulations at this temperature (Figure S11 a).

Model validation with independent experimental data sets at two extremes of particle size suggests that accurate, aggregated predictions are possible to describe pre-sieving feedstock behavior. Hence, kinetic experiments were then performed using bulk milled poplar in methanol at 220–250 °C for batch residence times of 2.0–20.0 min (Figure 7 and Figure S19). Separately, 2 D simulations that use each of the four representative particle sizes were performed under identical conditions. Kinetic profile responses for each particle size were aggregated by using a weighted-average sum based on known mass fractions of the corresponding sieve fractions (Figure S1). Ensemble responses in this manner were calculated for each temperature, and the results are shown alongside the experimental data in Figure 7 a and b and Figure S19. Excellent agreement is observed across all conditions (Figure 7 c). Although some underprediction is observed, ensemble model values exhibit no more than a 7 wt% residual error across all data. Thus, these ensemble calculations illustrate the high confidence of 2 D ROM predictions for a highly heterogeneous poplar feedstock.

Reaction–diffusion model extension to three dimensions

Given the validity and robustness of the 2 D ROMs, we next developed 3 D microstructural particle models. Compared to the 2 D systems, 3 D models invoke a related, albeit unique set of mass transport properties and assumptions that lead to nearly identical results for individual particles and ensembles. Briefly, isotropic effective diffusivity tensors are defined as per Equation (1) but with intra-cell-wall (CW) diffusion coefficients, $D_{CW,i}$, that incorporate Knudsen and molecular contributions for each species i. Further, tortuosities[38] and void fractions[39] were revisited to describe the cell wall, with values spanning 26 to 23 and 0.0015 to 0.0019, respectively, when scaled with the extent of extraction. See Supporting Information for full discussion of assumptions [Eqs. (S4)–(S7)] and 3 D tortuosity sensitivity analysis (Figure S20).

First, reaction–diffusion simulations were conducted for the 250–500 μm 3 D model. Mean best-fit kinetic parameters from the 2 D base case (Table 3) were applied to all 3 D models, and we adopted the reaction scheme described in Equation (5). Simulated extraction profiles for this particle size at the four temperatures are shown in Figure S21. Overall, predictions exhibit excellent agreement with the experimental data (Figure 2 a–d) and with the 2 D profiles (Figure S11 a–d). Microstructures further enable the visualization of intraparticle gradients,

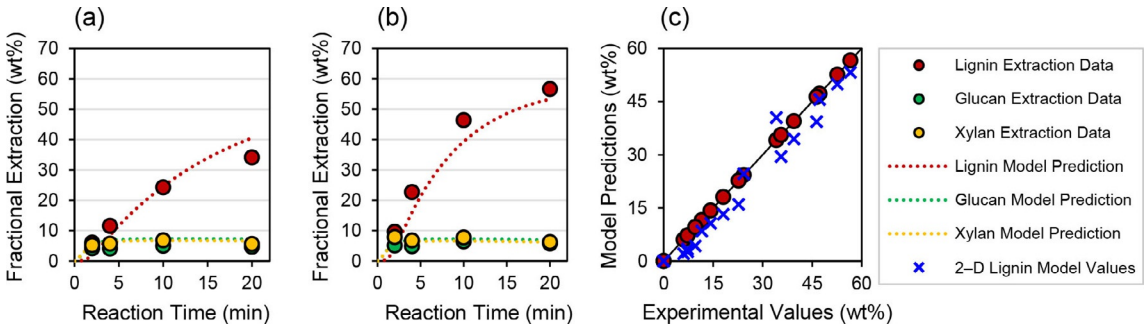

Figure 7. Time–course fractional extraction profiles for lignin, xylan, and glucan from experiments with bulk, pre-sieving poplar and from ensemble calculations by using 2D simulation responses summed across four particle sizes at a) 220 °C and b) 250 °C. c) Lignin extraction parity plot of 2D ensemble prediction values versus experimental data at 220–250 °C (see Figure S19 for time-course data and models at 230 and 240 °C). Experimental data points plotted reflexively along a 45° line (solid black line) for clarity.

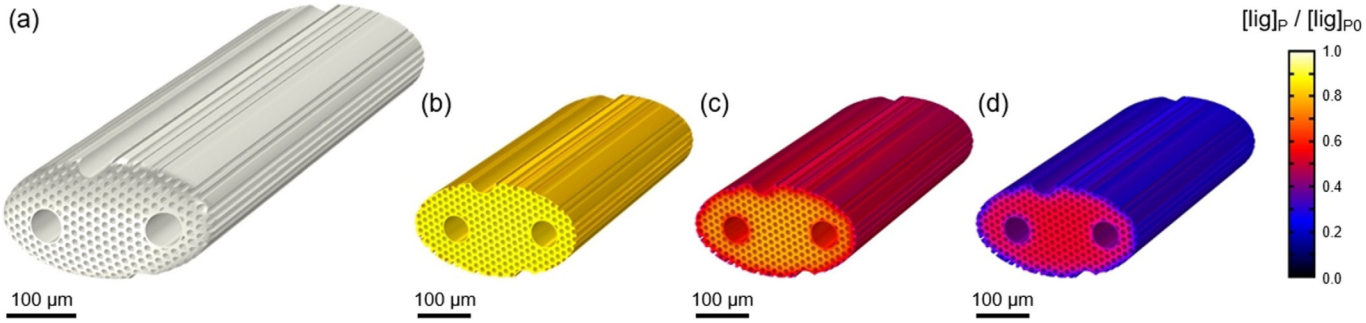

Figure 8. 3D microstructural model visualizations of lignin extraction at 250 °C from a representative 250–500 µm particle at various residence times *t*: a) full particle at *t* = 0 min, b) half particle at *t* = 4 min, c) half particle at *t* = 10 min, and d) half particle at *t* = 20 min. Half particles in b–d are used in reaction–diffusion simulations, and a symmetry boundary condition is enforced at the exposed interior radial face; the full particle in a is constructed from mirroring operations along this face. The color legend shown on the right is for dimensionless lignin concentration in the particle domain, $[lig]_P/[lig]_{P0}$. See Figure S21 d and videos A6 and A8.

and one such time–course lignin concentration map from a central radial slice of the particle interior at 250 °C is illustrated in Figure 8. In the absence of advection, cell wall lignin concentrations are higher in the particle interior than along the exterior edges, pore walls, and particle tips. Time–course particle animations of lignin extraction are included in Supporting Information video files A1–A12.

Ensemble calculations were next performed by a weighted summing of responses from each of the four representative 3D particles. Predictions presented in Figure S22 reveal excellent agreement with experimental data for bulk poplar, generating similar profiles to the 2D cases shown in Figure 7 and Figure S19. Taken together, 3D microstructural models are equally predictive of reaction–diffusion behaviors as the 2D ROMs, despite some key differences in mass transport assumptions for each model, which thus highlights the validity and utility of this complexity reduction.

Estimation of intra-cell-wall mass transfer resistance

Beyond ensembles, 3D models are practical to inform intrinsic kinetics relative to mass transfer limitations within cell wall domains. The Thiele modulus, ϕ, is a dimensionless number that describes the ratio of the reaction rate to the diffusion rate. Here, its expression for a first-order reversible reaction[40] is adapted to describe the lignin extraction–redeposition system of Equation (5). The forward and reverse reactions each involve different diffusing reactants within the cell wall, which requires distinct moduli to describe each process. We used Equations (6) and (7) to define Thiele moduli for the forward ($\phi_{f,CW}$) and reverse ($\phi_{r,CW}$) reactions, respectively:

$$\varphi_{f,CW} = \left(\frac{\text{reaction rate}}{\text{diffusion rate}}\right)_f^{\frac{1}{2}} = L\sqrt{\frac{k'_{lig,f}}{D_{e,MeOH}X_{lig,max}}} \quad (6)$$

$$\varphi_{r,CW} = \left(\frac{\text{reaction rate}}{\text{diffusion rate}}\right)_r^{\frac{1}{2}} = L\sqrt{\frac{k_{lig,r}}{D_{e,lig}X_{lig,max}}} \quad (7)$$

in which L is the characteristic length [m], $k'_{lig,f}$ [Eq. (6)] is the pseudo-first-order lignin extraction rate constant [s^{-1}], $k_{lig,r}$ [Eq. (7)] is the pseudo-first-order lignin redeposition rate constant [s^{-1}], and $X_{lig,max}$ is the dimensionless maximum extent of fractional extraction, bounded by 0 and 1. Each of these terms is described in detail next. Lastly, reactant effective diffusivities $D_{e,MeOH}$ [Eq. (6)] and $D_{e,lig}$ [Eq. (7)] are defined by Equations (1) and (S5) [$m^2 s^{-1}$], respectively.

For intra-cell-wall reaction and diffusion, the characteristic length L is taken as 2.1 μm, the mean fiber cell wall thickness (Table 2). Conceptually, this value represents the hypothetical mean path length required for methanol diffusion from lumen to compound middle lamella in the forward reaction, or for lignin fragment diffusion from compound middle lamella to lumen in the reverse reaction (Figure S5 and Figure 8). Notably, the fiber cell wall thicknesses measured for this poplar vary with a standard deviation of ±0.6 μm (±29%; Table 2), which implies that broad ranges of L, and thus of $\phi_{f,CW}$ and $\phi_{r,CW}$, likely exist within any real feedstock.

Next, $k'_{lig,f}$ [s^{-1}] can be derived from the pseudo-second-order rate constant $k_{lig,f}$ [$m^3\,mol^{-1}\,s^{-1}$]. Specifically, the forward reaction of Equation (5) describes a pseudo-second-order extraction, wherein native lignin immobilized in the cell wall undergoes extraction by methanol. Thus, the forward Thiele modulus $\phi_{f,CW}$ must relate reaction and diffusion with respect to the mobile methanol reactant. Accordingly, the product of $k_{0,lig,f}$*[lig]$_0$ yields a pseudo-first-order pre-exponential factor $k'_{0,lig,f}$, from which the pseudo-first-order rate constant $k'_{lig,f}$ [s^{-1}] may be calculated for a given temperature T from the corresponding $E_{a,lig,f}$ values from Table 3. In contrast, the reverse reaction of Equation (5) captures lignin redeposition described by the pseudo-first-order rate constant $k_{lig,r}$ [s^{-1}] without further adaptation.

Finally, as a result of the redeposition of lignin, the Thiele modulus is scaled by the maximum extent of extraction of this species, $X_{lig,max}$. Such extents are determined by performing 2D simulations at long residence times (Figure S23) and are analogous to equilibrium conversion values in isothermal, homogeneous kinetic systems; however, exponential-like decay is observed in lignin extraction profiles after quasi-equilibrated maximum extraction values are reached, akin to the rapid consumption of an intermediate product of series reactions. This behavior is reflected quantitatively in the intrinsic selectivity ratio of $k''_{lig,f}/k_{lig,r}$, in which $k''_{lig,f}$ is the product of $k_{lig,f}$ and [MeOH]$_0$, with ratios that span 0.15–0.21 across multiple temperatures and solute identities (Table S5). The deviation from traditional equilibrium kinetic behavior indicates that the redeposition reaction rate dominates at long residence times, likely as a consequence of enhanced fluid-phase diffusion at final reaction temperatures and at high solution concentrations of extracted lignin. Thus, in lieu of an equilibrium extraction value, $X_{lig,max}$ is used as a scaling factor in Equations (6) and (7) to account for incomplete lignin extraction.

Values of each Thiele modulus and of $X_{lig,max}$ for the 250–500 μm 3D model across a range of temperatures and solute sizes are given in Table 4. The terms $k'_{lig,f}$, $k_{lig,r}$, $D_{e,MeOH}$, and $D_{e,lig}$ are evaluated at final temperatures after reactor heat-up, and initial values of [lig]$_P$ (250 mol m^{-3} poplar for lignin dimers, 152 mol m^{-3} for tetramers, and 54.7 mol m^{-3} for decamers) are assumed for the calculation of the kinetic term in $\phi_{f,CW}$. Processes with Thiele moduli of $\phi < 0.40$ are considered to be kinetically limited, whereas values in the range of $0.40 < \phi < 4.0$ correspond to competing reactive and diffusive phenomena.[40b] All $\phi_{f,CW}$ values are very small (< 0.04), which suggests that methanol reaction with cell wall lignin is limited entirely by its intrinsic kinetics; this finding is expected given the small size of the reactant. However, the resulting values of $\phi_{r,CW}$ are in the range of 0.55–1.43, which indicates that reaction and diffusion processes for methanolyzed lignin fragments indeed compete on the same time and length scales inside poplar cell walls. Generally, $\phi_{r,CW}$ trends with increasing temperature (i.e., faster kinetics) and with increasing solute size (i.e., slower diffusion), with the largest value of 1.43 observed for decamer extraction at 250 °C. Lignin speciation trends are also reflected in increasing $X_{lig,max}$ and in longer residence times t_{max} required to reach such extents for heavier solutes (Table 4), which implies that fluid-phase diffusion of extracts also influences apparent redeposition rates.

Table 4. Calculated values of intra-cell-wall forward Thiele modulus $\phi_{f,CW}$, reverse Thiele modulus $\phi_{r,CW}$, and effectiveness factors $\eta_{f,CW}$ and $\eta_{r,CW}$ for lignin dimer, tetramer, and decamer extractions from 250–500 μm poplar.[a] Maximum extent of lignin extraction $X_{lig,max}$ and associated residence time t_{max} are reported for each case.

Lignin speciation	T [°C]	$\phi_{f,CW}$[b]	$\eta_{f,CW}$[b,d]	$\phi_{r,CW}$[c]	$\eta_{r,CW}$[c,d]	$X_{lig,max}$[e]	t_{max}[e] [min]
dimer[f]	220	0.015	>0.99	0.55	0.91	0.52	54.0
	250	0.031	>0.99	0.72	0.86	0.55	30.0
tetramer[g]	220	0.011	>0.99	0.61	0.89	0.55	60.0
	250	0.015	>0.99	0.79	0.83	0.58	33.0
decamer[h]	220	0.008	>0.99	1.05	0.74	0.57	62.5
	250	0.010	>0.99	1.43	0.62	0.58	38.5

[a] Characteristic length L of 2.1×10^{-6} m for mean fiber cell wall thickness (Table 2). [b] See Equation (6) for forward Thiele modulus definition and text for discussion. [c] See Equation (7) for reverse Thiele modulus definition and text for discussion. [d] See Equation (8) for effectiveness factor definition and text for discussion. [e] See Figure S23 and text for discussion. [f] Rate constant and diffusion coefficient calculated for lignin dimer (436 Da) case at specified T. See Table 3, Figure 6, Figure S8b, and text for discussion. [g] Rate constant and diffusion coefficient calculated for lignin tetramer (715 Da) case at specified T. See Table 3, Figure 6, Figure S8c, and text for discussion. [h] Rate constant and diffusion coefficient calculated for lignin decamer (1992 Da) case at specified T. See Table 3, Figure 6, Figure S8d, and text for discussion.

The effectiveness factor, η, is another useful dimensionless metric to assess diffusion resistance in kinetic systems. The value of η ranges from 0 to 1, and the upper limit indicates no diffusion resistance. The first-order solution for a flat plate geometry is considered to be an adequate approximation for η in arbitrarily shaped geometries.[40b,41] Here, intra-cell-wall effectiveness factors $\eta_{f,CW}$ and $\eta_{r,CW}$ are defined by Equation (8):

$$\eta_{j,CW} = \frac{\tanh(\varphi_{j,CW})}{\varphi_{j,CW}} \tag{8}$$

in which the subscript j may refer to either the forward (f) or the reverse (r) reaction. The values of $\eta_{j,CW}$ for each case are listed in Table 4. Although all the values of $\eta_{f,CW}$ lie near unity as expected, $\eta_{r,CW}$ spans 0.91 to 0.62 as the solute size and temperature increases. Practically, the intra-cell-wall diffusion of liberated lignin may hinder apparent kinetic rates by up to approximately 40% at a high MW and high temperature.

Consequences of confinement: Intrapore mass transfer resistance

Lignin extracted from cell walls must traverse lumen within the greater poplar tissue structure to escape into free solution. Just as diffusion resistance inhibits intrinsic chemistries of extracted lignin inside of poplar cell walls, lignin mass transfer and the kinetics of extraction and redeposition further compete within these axial pores, which introduces the influence of particle size on observable productivities. The consequences of intrapore mass transfer resistance are now examined among the four representative poplar particles with extensions to large particle and extra-large bulk wood geometries.

First, reaction–diffusion models were extrapolated to these large-length geometries. If we take the representative 250–500 μm 2D particle model (1.07 mm average length; Figure 5) as a basis, larger 2D particles of identical aspect ratio were generated readily by isotropic scaling by factors of 2, 5, 10, and 20; the resulting particles exhibit average lengths of 2.14–21.4 mm. For comparison, porous sphere models of equivalent volume were created for each of these five particle sizes. Separately, extra-large geometries were generated for a representative wood chip[42] (1 cm thickness × 1.5 cm width × 3 cm length), analogous to paper and pulping feeds, and for a representative poplar 2"×4" plank (1.5" thickness × 3.5" width × 48" length), which is relevant to lumber delignification for the production of "super-wood"[9a] and optically transparent[9b] materials. Here, for illustration, these bulk 3D geometries assume the shape of rectangular prisms with uniform porosity (i.e., no explicit microstructure) with identical poplar/methanol volume ratios as in all other models and experiments. Overall, reaction kinetics, temperature profiles, and mass transfer properties follow all assumptions incorporated into the original base-case 2D particle models, and the key variable of poplar domain size now spans several orders of magnitude.

Time–course lignin extraction profiles are illustrated for these geometries at 250 °C in Figure 9a–c. As expected, apparent extraction rates and productivities trend inversely with the increase of the poplar domain size, and severe hindrances are observed for geometries that exceed approximately 5 mm lengths (Figure 9a and c). Domains above this threshold exhibit significant retardation and/or complete cessation of lignin extraction after approximately 5 min of reaction,[1] which suggests an inability of reactive lignin fragments to escape long poplar lumen. In contrast, simple porous sphere geometries yield higher predictions than rod-like particles in all cases except the smallest particle (Figure 9b), and dramatic differences are observed for the three largest particle analogues, which further reinforces the need for feedstock-relevant geometries.

Next, alternate forms of the Thiele modulus are defined for reaction–diffusion phenomena experienced by methanol and by methanol-extracted lignin fragments within the lumen of these various geometries. These intraparticle Thiele moduli, $\phi_{f,P}$ and $\phi_{r,P}$, follow the forms of Equations (6) and (7), respectively, with appropriate substitutions for the characteristic length L and for the effective diffusivities $D_{e,MeOH}$ and $D_{e,lig}$. Given the anisotropic nature of woody feedstocks, porous diffusion is favored heavily along the longitudinal axis.[34] Therefore, L is defined as half of the average particle length, determined for 2D axisymmetric ROMs as the mean of the center and edge boundary lengths (Figure 5). Accordingly, the effective diffusivities take the form of Equation (1) under the Darcy's law assumption of uniformly distributed porosity; notably, $D_{e,lig}$ is considered here only for tetrameric lignin solutes, although the most extreme effects are predicted for decamers. Pseudo-first-order rate constants $k'_{lig,f}$ and $k_{lig,r}$ (tetramer case only) and maximum extent of extraction $X_{lig,max}$ are defined as above. Lastly, analogous effectiveness factors, $\eta_{f,P}$ and $\eta_{r,P}$, may be defined as per the form of Equation (8) as functions of moduli $\phi_{f,P}$ and $\phi_{r,P}$, respectively.

The relationship between the intraparticle Thiele moduli and the average poplar domain length, $2L$, for the four representative milled poplar particles and for larger poplar structures simulated at 220 and 250 °C is illustrated in Figure 9d and Figure S24a. Generally, the Thiele modulus scales with poplar domain length across several orders of magnitude, which implies the significant dependence of intraparticle diffusion on particle and, hence, pore lengths, among other factors (see Table S6 for complete tabulations of L, $X_{lig,max}$, t_{max}, $\phi_{f,P}$, $\phi_{r,P}$, $\eta_{f,P}$, and $\eta_{r,P}$). Particles in this study and hypothetical large structures are seen to span the extremes of both kinetically limited (i.e., $[\phi_{f,P}, \phi_{r,P}] < 0.4$) and diffusion-limited (i.e., $[\phi_{f,P}, \phi_{r,P}] > 4.0$) regimes; the critical values of the domain length $2L$ for each $\phi_{r,P}$ threshold condition interpolated from power law best-fits [Eqs. (9) and (10)] are listed in Table 5. Analogous critical values of $2L$ for $\phi_{f,P}$ cases are listed in Table S7; see Equations (S8) and (S9). Further, calculated intraparticle effectiveness factors are illustrated in Figure 9e as a function of $\phi_{r,P}$ and in Figure S24b as a function of $\phi_{f,P}$. Values of $\eta_{r,P}$ range from near unity for the two smallest particles to approximately 10^{-4} for the 2"×4" poplar plank, indicative of a transition into extraordinary diffusion resistances among medium to large structures; a similar span is observed for $\eta_{f,P}$ (Figure S24b and Table S6). Several crucial insights are gleaned from these trends:

1. Typical particles representative of milling through a 2 mm screen (i.e., $2L$ in the range 0.34–1.4 mm; Table S6) lie in the intermediate regime (i.e., $0.4 < \phi_{r,P} < 4.0$) in which lignin fragment reaction and diffusion compete on the same time and length scales;

[0] *Simulations depicted in Figure 9c for the poplar chip and plank abide by all assumptions developed for base-case 2D ROMs. Although the assumption of complete methanol pore infiltration at $t = 0$ is representative of batch reactor experiments with milled poplar, this scenario is likely not applicable to bulk poplar geometries, given the substantially larger path lengths (and, hence, residence times) required for solvent diffusion and infiltration. However, for il-*

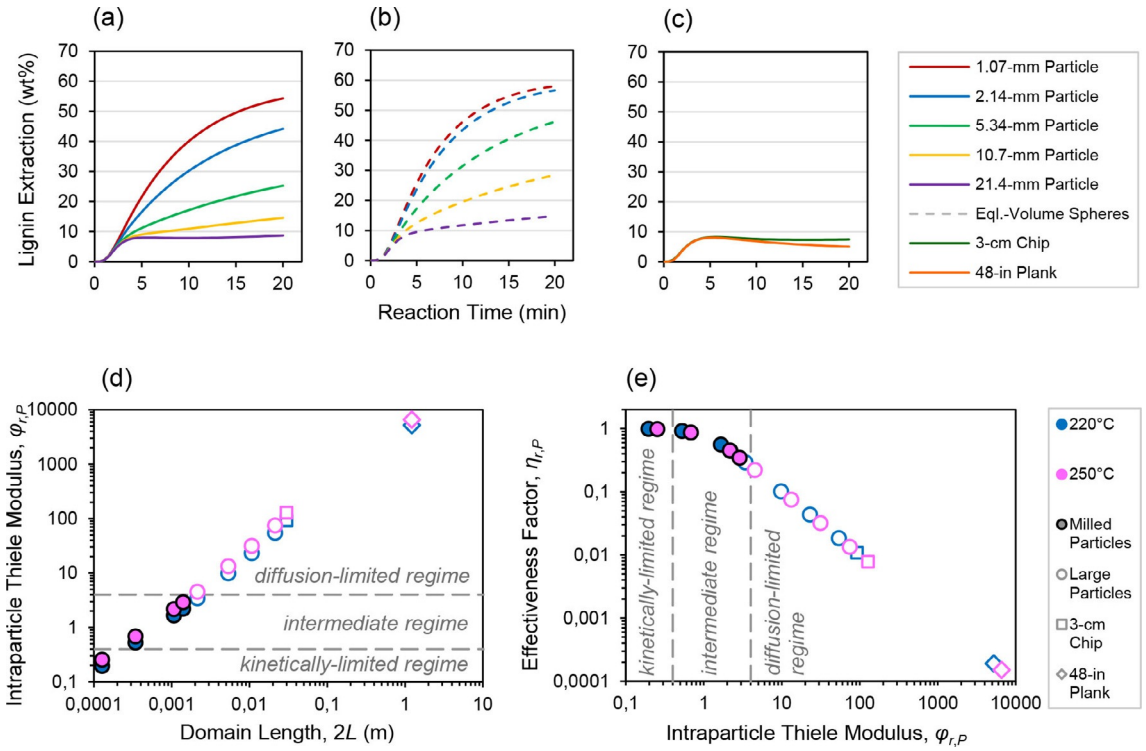

Figure 9. Lignin extraction profiles and mass transfer consequences of poplar domain size. a) Time–course lignin extraction profiles at 250 °C for 2D axisymmetric particles of varying average length; large particles generated by isotropic scaling of the 1.07 mm model. b) Time–course lignin extraction profiles at 250 °C for 2D axisymmetric spheres of equivalent volumes to each corresponding particle; color legend same as in a. c) Time–course lignin extraction profiles at 250 °C for 3D bulk geometries. d) Relationship between intraparticle reverse Thiele modulus, $\phi_{r,P}$, and average poplar domain length, $2L$, for various poplar geometries evaluated at 220 and 250 °C. e) Relationship between the intraparticle reverse effectiveness factor, $\eta_{r,P}$, and intraparticle reverse Thiele modulus, $\phi_{r,P}$, for poplar domains evaluated at 220 and 250 °C. Dashed lines in d and e indicate boundaries between key reaction–diffusion regimes labeled by inset text boxes: kinetically limited regime ($\phi_{r,P} < 0.4$), intermediate regime ($0.4 < \phi_{r,P} < 4.0$), and diffusion-limited regime ($\phi_{r,P} > 4.0$).[40b] See Table S6 for complete $\phi_{r,P}$ and $\eta_{r,P}$ inputs and text for parameter definitions.

2. Poplar domains with $2L$ larger than approximately 2 mm (Table 5) are predicted to be entirely diffusion-limited for phenomena that involve lignin fragments, such that strong resistance to lumen diffusion limits lignin extraction rates overwhelmingly. The corresponding effectiveness factors of $\eta_{r,P} < 0.25$ suggest that any apparent (i.e., observable) kinetic measurements for $2L > \approx 2$ mm will be at least 75% erroneous;
3. Extremely fine poplar particles ($2L < \approx 0.2$ mm; Table 5) are required to completely avoid the diffusion limitations associated with extracted lignin; and
4. The methanol reaction is overall significantly less hindered by mass transfer resistance, although reaction and diffusion are observed to compete along the same scales (i.e., $0.4 < \phi_{f,P} < 4.0$) for the chip and for particles with $2L > \approx 10$ mm (Figure S24 and Tables S6–S7). Diffusion limitations completely control (i.e., $\phi_{f,P} > 4.0$) methanol extraction of the 2"×4" plank.

Practically, these insights inform the dominant role of intraparticle mass transfer resistance in hampering apparent lignin extraction rates.

Table 5. Critical poplar domain lengths, $2L_{crit}$, that correspond to intraparticle reverse Thiele modulus thresholds for kinetically limited ($\phi_{r,P} < 0.4$) and diffusion-limited ($\phi_{r,P} > 4.0$) regimes at 220 and 250 °C.

T [°C]	$2L_{crit}$ [mm]	$\phi_{r,P}$	Physical interpretation
220[a]	0.24	0.4	no resistance to lumen diffusion for $2L < 2L_{crit}$
220[a]	2.4	4.0	strong resistance to lumen diffusion for $2L > 2L_{crit}$
250[b]	0.18	0.4	no resistance to lumen diffusion for $2L < 2L_{crit}$
250[b]	1.8	4.0	strong resistance to lumen diffusion for $2L > 2L_{crit}$

[a] $2L_{crit}$ values at 220 °C interpolated from best-fit power law relationship $\phi_{r,P} = 4059 \times (2L\ [m])^{1.129}$ [Eq. (9)] determined from regression of data in Figure 9d. [b] $2L_{crit}$ values at 250 °C interpolated from best-fit power law relationship $\phi_{r,P} = 5412 \times (2L\ [m])^{1.130}$ [Eq. (10)] determined from regression of data in Figure 9d.

Discussion

The current work predicts that mass transfer in plant cell walls and in particle pores plays a definitive role in lignin-first extraction processes. Several actionable insights are discussed below to guide future investigations in these fields.

Variables to control the Thiele modulus

We now reconsider the Thiele modulus in the context of tunable laboratory parameters to address diffusion limitations. Here, the forms of Equations (6) and (7) are applicable to both intra-cell-wall and intraparticle domains, and we made appropriate substitutions for L, $D_{e,MeOH}$, and $D_{e,lig}$ in each case (vide supra). Insights and opportunities are discussed for each contributing term in the Thiele modulus.

Characteristic length, L

The characteristic lengths of the cell wall thickness (i.e., for $\phi_{f,CW}$ and $\phi_{r,CW}$) and of the particle domain half-length (i.e., for $\phi_{f,P}$ and $\phi_{r,P}$) raise important questions about biomass cultivation and mechanical processing. For a given species, the plant cell wall thickness is a function of genetic, environmental, and seasonal factors;[43] however, optimal growth and cultivation conditions generally favor heartier, thicker-walled cells, which necessarily introduce longer diffusion path lengths for reactants and extracted intermediates. Further, different cultivation conditions will likely produce a wide range of cell wall thicknesses and lumen diameters (Table 2, Figures S5 and S7), which lead to a diversity of characteristic lengths for diffusion and reaction.

Particle domain lengths, however, are tuned practically by mechanical refining, which offers a handle to control intraparticle diffusion limitations. An important cost driver in most biomass valorization schemes is the degree of mechanical refining, an often energy-intensive[44] step with implications for downstream processing (e.g., solids handling, pressure drops, yields). The impractical extent of refining required to eliminate intraparticle diffusion resistances completely is summarized in Table 5 and Table S7. This implies the need to address this challenge with any reasonably sized feedstock, particularly for any large sizes (e.g., wood flakes, slivers, pellets, chips, and lumber) that exceed standard milled particle ranges used commonly by laboratory researchers. The crucial trade-off between the apparent yield of a feedstock form and its ease of handling in lignin-first biorefining is illuminated perhaps most clearly by the governing role of mass transfer, and future investigations and scale-up efforts should account for transport phenomena to achieve optimal throughput and product yield.

Intrinsic rate constants, $k'_{lig,f}$ and $k_{lig,r}$

Although primary solvolytic chemistries (e.g., the reaction of methanol with cell wall lignin) are not predicted to have diffusion limitations inside the cell wall (Table 4) with minimal resistance inside of pores (Figure S24 and Table S6), secondary redeposition reactions compete with mass transfer both inside of cell walls (Table 4) and in particle lumen (Figure 9d and e and Table S6). Redeposition rate terms are especially dominant over those that describe primary lignin methanolysis events (Table S5). The corresponding intrinsic rate constants are strong functions of temperature [Eq. (5)], although this experimental handle is limited in utility to decouple and mitigate mass transfer resistances (Table 4, Table S6, Figure 9d, and Figure S24a), particularly if thermal gradients are present. Instead, solvent(s) play a pivotal role in the generation, stabilization, and transport of reactive solvolysis intermediates. For example, different solvent environments engender different lignin conformations.[45] Separately, others have observed broad differences in solvolysis[46] and in batch RCF[47] yields if different solvents are employed.

On the molecular scale, the type and abundance of side- and end-chain functionalities[13b,c,48] as well as interaromatic linkage diversity impact the intrinsic reactivity of the oligomer with protic solvents as well as its autoreactivity and adsorptivity[49] to undergo recondensation and/or redeposition chemistries. Resilience against these undesired reactions may also be fortified by employing protecting group chemistry[50] to stabilize extracted lignin oligomers, which effectively lowers $k_{lig,r}$ and thus both $\phi_{r,CW}$ and $\phi_{r,P}$. Notably, active stabilization strategies that invoke solid heterogeneous catalysts are not relevant to the decrease of $k_{lig,r}$ as redeposition chemistries occur within biomass cell walls and pores independently of solid catalyst phases. Research into mesoscale lignin stabilization routes to mitigate redeposition is encouraged, particularly with attention to the competing mass transport phenomena.

Effective diffusivities, $D_{e,MeOH}$ and $D_{e,lig}$

Diffusion coefficients are moderate functions of temperature (Figure 6 and Figure S8), although the acceleration of the diffusion of a reactive species at higher temperatures necessarily accelerates the intrinsic kinetics of its generation (Figure S10 and Table S6) and consumption (Table 4 and Table S6). Therefore, diffusivities are perhaps more effectively modulated by solvent identity, solvent/solute size (i.e., MW), pore size (i.e., lumen diameter), and solute construction (i.e., oligomer linkages, branching, etc.). Solute and lumen sizes are difficult to control narrowly, given the large distributions observed for each within the single poplar feedstock studied here (Table 2, Table S3, Figure 1c and 3b, and Figures S5 and S7); however, genetic engineering may afford opportunities to change tissue structure and cell wall architecture in hardwoods[51] to allow more open hierarchical pore structures (i.e., increased void fraction ε_P and reduced tortuosity τ) in which solute diameters are relatively small compared to those of vessel lumen. Other feedstocks, such as softwoods or herbaceous crops, will engender their own distinct structural features with analogous opportunities to enhance the diffusivity.

Separately, lignin solute synthesis and composition may be readily controlled by tuning in planta,[52] such as by the utilization of different S/G/H ratios from natural[53] and transgenic[54] variants and/or by the incorporation of alternate monolignols during biosynthesis.[55] At the mesoscale, chain length,[56] branching,[28c,57] and solvated oligomer conformations[28c,45] are most influential to modulate molecular diffusivities. These characteristics are necessarily also functions of intermolecular forces, solvent(s), co-solutes, additives, biomass surface properties, and temperature but may offer future avenues for biochemical research and development.

Maximum extent of fractional extraction, $X_{lig,max}$

The final parameter in the Thiele moduli is $X_{lig,max}$, the maximum extent of lignin extraction, although parallels may be drawn for other reactive species of interest to related systems. This dimensionless measure of extraction productivity is closely related to $k'_{lig,f}$, $k''_{lig,f}$, and $k_{lig,r}$, and by analogy it may be augmented by in situ lignin protection and stabilization approaches discussed above as strategies to reduce $k_{lig,r}$. Alternately, $X_{lig,max}$ may be increased by enhancing the extractability of lignin inside of cell walls, which affords opportunities in tailored lignin biosynthesis and tuning in planta[58] to target lignin localizations, compositions, and local solvent environments that are most amenable to high extraction extents; separate preprocessing strategies such as steam explosion[7b] or other exfoliative techniques may further enable more rapid extraction kinetics with higher $k'_{lig,f}$ and $X_{lig,max}$.

However, lignin redeposition rates naturally counteract solvolytic extraction rates. Redeposition is particularly dominant at high extents of extraction (Figure S23) because this relative rate is dependent on the solution-phase concentration of lignin, $[lig]_S$ [Eq. (5)]. Nonetheless, the solute concentration local to an external particle surface may be reduced significantly upon the introduction of flow gradients [i.e., by adding advection terms to Eqs. (3) and (4)]. The continuous removal of lignin fragments effectively lowers local concentrations at external surfaces to minimize rates of undesired reactions, and it also maintains high local fluxes and high concentration gradients, the driving forces for bulk-phase mass transfer. Practically, agitation and baffling in stirred vessels or convective flow in tubular reactors may accomplish continuous, uniform lignin removal at these external surfaces and are expected to improve maximum extents of lignin extraction, often observed to reach up to approximately 70% delignification for typical RCF processes.[47a] However, external (i.e., film) mass transfer during convection is not predicted to control effective rates of lignin extraction if film transport rates are compared to those of surface reactions and underlying internal mass transfer resistances [Table S8; see Eq. (S10) and Supporting Information for discussion]. Other complex mixing phenomena, such as pocketing, channeling, back-mixing, thermal non-uniformities, or Rayleigh–Bénard convection, may further cause diffusivities, reaction rates, concentration gradients, and velocity gradients to vary with space and time at the reactor scale.[59] Overall, the exploration of strategies to improve $X_{lig,max}$ to reduce $\phi_{r,CW}$, $\phi_{f,P}$, and $\phi_{r,P}$ will identify numerous options to maximize lignin removal from feedstocks and to simultaneously enhance bulk-phase mass transfer.

Additional insights for biomass practitioners

Beyond variables that affect the Thiele modulus directly, this section highlights additional points for the lignin-first biorefining research community.

First, the nature of lignin and of its molecular diversity is a well-known, albeit complex, determinant of its valorization potential.[1c] The incorporation of select and/or alternate monolignols into lignin backbones can influence chain length,[56] side- and end-chain functionalization,[55a,60] cross-linking with polysaccharides,[61] and localization within cell walls,[58,62] each of which, in turn, influences its physical accessibility to extraction solvents and the resulting chemical reactivity in those processes. MD simulations and related lignin computational tools[28,55b] are able to predict solvation and diffusivity behaviors in myriad chemical environments, which thus connects experimental insights with predictive, molecular-scale physics. Insights from the mesoscale models presented here motivate these and other strategies to tune lignin biosynthesis and cellular localizations for optimal mass transfer and chemical extraction at the particle scale.

For plant biologists and wood material scientists, reaction–diffusion models are well suited to connect feedstock material attributes to their engineering performance. For hardwoods, cellular-scale phenotyping of features such as fiber cell wall thickness, lumen diameter, spatial frequency of vessel cells, and transverse tissue features can help to identify and predict differences in mass transport phenomena among natural variants and/or transgenic plants. Further, identification of genetic clusters and predictors for cell length, vessel cell abundance in hardwoods, and other mesoscale porosity features from genome-wide association study (GWAS) populations will highlight avenues to engineer next-generation feedstocks for optimal deconstruction and upgrading.[63] Lastly, material properties of woody materials immersed in organic solvents are deserving of attention from the materials science community, as these characteristics inform important heat and mass transport descriptors relevant to chemical processing. Of specific relevance to biomass processing is understanding and developing cell-wall-specific diffusivity models that may represent the physics of local microenvironments within plant tissues more accurately. Analogous opportunities may exist to cater to engineered softwoods and herbaceous feedstocks.

For biomass conversion researchers, there are many variables in lignin valorization experiments, particularly if heterogeneous catalysts are employed. However, feedstock variability has substantial consequences for lignin solvolysis. This variability generally refers to internal microstructural diversities (Table 2 and Figures S5 and S7), external particle geometries (Table 1) and morphologies (Figure S4), particle size distributions resulting from typical size reductions (Figures S1 and S6), and batch-to-batch, plant-to-plant, tissue-to-tissue, and species-to-species variations, all of which portend macroscale implications for lignin uniformity, extractability, and upgradability, as well as for general reproducibility within and among proposed strategies.

The results presented in Figure 9d–e and Tables 4 and 5 and Table S6 suggest that much lignin-first research has been conducted in the presence of mass transfer limitations that, at best, compete directly with underlying reactive processes. Further, RCF reactions performed in standard pressure vessels experience heat-up periods often on the order of approximately 0.5–1.0 h, which obscures the interpretation of kinetic data. To link lignin model compound studies to real biomass, very fine feedstock particles must be used to assess true kinetic behav-

iors or catalyst-phase limitations (Table 5); conversely, the use of any realistic feedstock size ranges must be accompanied by thorough, relevant diagnostic experiments to assess the mass transfer resistances[21,41] within biomass and catalyst solids, in addition to accounting for common reactor-scale non-isothermalities. The design, evaluation, and deployment of lignin-first and other biorefining catalysts will be best enabled by overcoming the limitations of biomass itself.

Conclusions

Through the development of mesoscale reaction–diffusion models for lignin-first fractionation, we predict that mass transfer plays a governing role in solvolytic lignin extraction at the mesoscale, and the reaction and diffusion of lignin fragments compete along the same time and length scales within cell walls and lumen for typical milled particles. Such systems are predicted to be entirely diffusion-limited if characteristic domain lengths exceed as little as approximately 2 mm. These findings elucidate critical thresholds for the mechanical refining of feedstocks necessary to avoid diffusion limitations entirely at very small ($<\approx 0.2$ mm) particle sizes; however, given the impracticality of the use of fine particles outside of laboratory settings, intra-biomass transport phenomena must be considered in lignin-first and related biorefining processes.

Particle-scale modeling and the accompanying kinetic experiments are demonstrated here for the exemplary fractionation of lignin-first solvolysis but may be retooled straightforwardly for virtually any condensed-phase biomass pretreatment technology. Overall, these predictive capabilities connect key feedstock material attributes to engineering performance, which allow fundamental, cellular-level insights from plant biology to better enable and guide chemical process research and development across multiple time and length scales. Further, practical strategies may be readily identified in real reactor systems to optimize hydrodynamics, contacting patterns, and key cost drivers, such as reactor capital requirements, process severity (*T*, *P*), residence times, and solvent demands. The untangling of heat, mass, and momentum transfer from chemical kinetics is vital in the pathways to scale-up and commercialization. The reaction–diffusion models presented in this work are intended to help lay the foundation for these future frontiers in biorefining.

Acknowledgements

This work was authored in part by researchers at the National Renewable Energy Laboratory, operated by the Alliance for Sustainable Energy, LLC, for the U.S. Department of Energy (DOE) under Contract No. DE-AC36-08GO28308. Funding was provided by the U.S. Department of Energy, Office of Energy Efficiency and Renewable Energy, Bioenergy Technologies Office. We thank Wouter Schutyser, Vivek Bharadwaj, Aaron Lattanzi, Michael Crowley, Jacob Kruger, Michael Stone, Eric Anderson, Lauren Dellon, Brenna Black, Ashutosh Mittal, Gerald Tuskan, and Aditya Bhan for their helpful discussions.

Conflict of interest

The authors declare no conflict of interest.

Keywords: biomass reaction kinetics · computational fluid dynamics · reductive catalytic fractionation · solvolysis · transport phenomena

[1] a) W. Schutyser, T. Renders, S. Van den Bosch, S. F. Koelewijn, G. T. Beckham, B. F. Sels, *Chem. Soc. Rev.* **2018**, *47*, 852–908; b) Z. Sun, B. Fridrich, A. de Santi, S. Elangovan, K. Barta, *Chem. Rev.* **2018**, *118*, 614–678; c) R. Rinaldi, R. Jastrzebski, M. T. Clough, J. Ralph, M. Kennema, P. C. A. Bruijnincx, B. M. Weckhuysen, *Angew. Chem. Int. Ed.* **2016**, *55*, 8164–8215; *Angew. Chem.* **2016**, *128*, 8296–8354.
[2] C. J. Biermann in *Handbook of Pulping and Papermaking, 2nd ed.* (Ed.: C. J. Biermann), Academic Press, San Diego, **1996**, pp. 55–100.
[3] S. Constant, H. L. J. Wienk, A. E. Frissen, P. d. Peinder, R. Boelens, D. S. van Es, R. J. H. Grisel, B. M. Weckhuysen, W. J. J. Huijgen, R. J. A. Gosselink, P. C. A. Bruijnincx, *Green Chem.* **2016**, *18*, 2651–2665.
[4] a) P. Sannigrahi, A. J. Ragauskas in *Aqueous Pretreatment of Plant Biomass for Biological and Chemical Conversion to Fuels and Chemicals* (Ed.: C. E. Wyman), Wiley, Chichester, UK, **2013**, pp. 201–222; b) Z. Zhang, M. D. Harrison, D. W. Rackemann, W. O. S. Doherty, I. M. O'Hara, *Green Chem.* **2016**, *18*, 360–381.
[5] J. S. Kim, Y. Y. Lee, T. H. Kim, *Bioresour. Technol.* **2016**, *199*, 42–48.
[6] A. George, A. Brandt, K. Tran, S. M. S. N. S. Zahari, D. Klein-Marcuschamer, N. Sun, N. Sathitsuksanoh, J. Shi, V. Stavila, R. Parthasarathi, S. Singh, B. M. Holmes, T. Welton, B. A. Simmons, J. P. Hallett, *Green Chem.* **2015**, *17*, 1728–1734.
[7] a) S. Ewanick, R. Bura in *Bioalcohol Production* (Ed.: K. Waldron), Woodhead Publishing, **2010**, pp. 3–23; b) A. Duque, P. Manzanares, I. Ballesteros, M. Ballesteros in *Biomass Fractionation Technologies for a Lignocellulosic Feedstock Based Biorefinery* (Ed.: S. I. Mussatto), Elsevier, Amsterdam, **2016**, pp. 349–368.
[8] M. E. Himmel, S.-Y. Ding, D. K. Johnson, W. S. Adney, M. R. Nimlos, J. W. Brady, T. D. Foust, *Science* **2007**, *315*, 804–807.
[9] a) J. Song, C. Chen, S. Zhu, M. Zhu, J. Dai, U. Ray, Y. Li, Y. Kuang, Y. Li, N. Quispe, Y. Yao, A. Gong, U. H. Leiste, H. A. Bruck, J. Y. Zhu, A. Vellore, H. Li, M. L. Minus, Z. Jia, A. Martini, T. Li, L. Hu, *Nature* **2018**, *554*, 224; b) H. Zhu, Z. Fang, Z. Wang, J. Dai, Y. Yao, F. Shen, C. Preston, W. Wu, P. Peng, N. Jang, Q. Yu, Z. Yu, L. Hu, *ACS Nano* **2016**, *10*, 1369–1377; c) G. Chen, T. Li, C. Chen, C. Wang, Y. Liu, W. Kong, D. Liu, B. Jiang, S. He, Y. Kuang, L. Hu, *Adv. Funct. Mater.* **2019**, *29*, 1902772.
[10] J. M. Pepper, Y. W. Lee, *Can. J. Chem.* **1969**, *47*, 723–727.
[11] M. V. Galkin, J. S. M. Samec, *ChemSusChem* **2016**, *9*, 1544–1558.
[12] a) T. Renders, S. Van den Bosch, S. F. Koelewijn, W. Schutyser, B. F. Sels, *Energy Environ. Sci.* **2017**, *10*, 1551–1557; b) T. Renders, G. Van den Bossche, T. Vangeel, K. Van Aelst, B. Sels, *Curr. Opin. Biotechnol.* **2019**, *56*, 193–201.
[13] a) E. M. Anderson, M. L. Stone, M. J. Hülsey, G. T. Beckham, Y. Román-Leshkov, *ACS Sustainable Chem. Eng.* **2018**, *6*, 7951–7959; b) I. Kumaniaev, E. Subbotina, J. Savmarker, M. Larhed, M. V. Galkin, J. S. M. Samec, *Green Chem.* **2017**, *19*, 5767–5771; c) Y. Li, B. Demir, L. M. Vázquez Ramos, M. Chen, J. A. Dumesic, J. Ralph, *Green Chem.* **2019**, *21*, 3561–3572.
[14] a) E. Minami, S. Saka, *J. Wood Sci.* **2003**, *49*, 0073–0078; b) E. Minami, S. Saka, *J. Wood Sci.* **2005**, *51*, 395–400; c) J. Yamazaki, E. Minami, S. Saka, *J. Wood Sci.* **2006**, *52*, 527–532.
[15] a) M. Goto, J. M. Smith, B. J. McCoy, *Ind. Eng. Chem. Res.* **1990**, *29*, 282–289; b) B. R. You, S. C. Oh, *Korean J. Chem. Eng.* **2010**, *27*, 1159–1163; c) L. Li, E. Kiran, in *Supercritical Fluid Science and Technology, Vol. 406*, American Chemical Society, **1989**, pp. 317–331.
[16] K. M. F. Kazi, H. Gauvin, P. Jollez, E. Chornet, *Tappi J.* **1997**, *80*, 209–219.
[17] M. B. Pecha, J. I. M. Arbelaez, M. Garcia-Perez, F. Chejne, P. N. Ciesielski, *Green Chem.* **2019**, *21*, 2868–2898.
[18] a) C. Igathinathane, L. O. Pordesimo, E. P. Columbus, W. D. Batchelor, S. Sokhansanj, *Comput. Electron. Agr.* **2009**, *66*, 147–158; b) P. N. Ciesielski, M. F. Crowley, M. R. Nimlos, A. W. Sanders, G. M. Wiggins, D. Robichaud, B. S. Donohoe, T. D. Foust, *Energy Fuels* **2015**, *29*, 242–254.

[19] T. D. Goddard, C. C. Huang, E. C. Meng, E. F. Pettersen, G. S. Couch, J. H. Morris, T. E. Ferrin, *Protein Sci.* **2018**, *27*, 14 – 25.
[20] M. B. Pecha, E. Ramirez, G. M. Wiggins, D. Carpenter, B. Kappes, S. Daw, P. N. Ciesielski, *Energy Fuels* **2018**, *32*, 10683 – 10694.
[21] a) E. E. Petersen, *Chem. Eng. Sci.* **1965**, *20*, 587 – 591; b) D. E. Mears, *Ind. Eng. Chem. Process Des. Dev.* **1971**, *10*, 541 – 547.
[22] a) S. Cheng, I. D'cruz, M. Wang, M. Leitch, C. Xu, *Energy Fuels* **2010**, *24*, 4659 – 4667; b) H.-L. Yan, Z.-K. Li, Z.-C. Wang, Z.-P. Lei, S.-B. Ren, C.-X. Pan, Y.-J. Tian, S.-G. Kang, J.-C. Yan, H.-F. Shui, *Fuel* **2019**, *246*, 394 – 401.
[23] R. J. A. Gosselink, A. Abächerli, H. Semke, R. Malherbe, P. Käuper, A. Nadif, J. E. G. van Dam, *Ind. Crops Prod.* **2004**, *19*, 271 – 281.
[24] A. Sluiter, B. Hames, R. Ruiz, C. Scarlata, J. Sluiter, D. Templeton, D. Crocker, National Renewable Energy Laboratory, Technical Report NREL/TP-510 – 42618, **2008**.
[25] B. S. Donohoe, P. N. Ciesielski, T. B. Vinzant, in *Biomass Conversion: Methods and Protocols* (Ed.: M. E. Himmel), Humana Press, Totowa, NJ, **2012**, pp. 31 – 47.
[26] N. Gierlinger, M. Schwanninger, *Plant Physiol.* **2006**, *140*, 1246 – 1254.
[27] a) M. de Meijer, P. van der Zwan Rick, H. Militz, *Holzforschung* **1996**, *50*, 135 – 143; b) A. J. Jacobson, S. Banerjee, *Holzforschung* **2006**, *60*, 59 – 63.
[28] a) J. V. Vermaas, L. Petridis, J. Ralph, M. F. Crowley, G. T. Beckham, *Green Chem.* **2019**, *21*, 109 – 122; b) L. D. Dellon, A. J. Yanez, W. Li, R. Mabon, L. J. Broadbelt, *Energy Fuels* **2017**, *31*, 8263 – 8274; c) J. V. Vermaas, L. D. Dellon, L. J. Broadbelt, G. T. Beckham, M. F. Crowley, *ACS Sustainable Chem. Eng.* **2019**, *7*, 3443 – 3453.
[29] a) O. Guvench, S. N. Greene, G. Kamath, J. W. Brady, R. M. Venable, R. W. Pastor, A. D. MacKerell, Jr., *J. Comput. Chem.* **2008**, *29*, 2543 – 2564; b) O. Guvench, E. Hatcher, R. M. Venable, R. W. Pastor, A. D. MacKerell, *J. Chem. Theory Comput.* **2009**, *5*, 2353 – 2370.
[30] a) K. Vanommeslaeghe, E. Hatcher, C. Acharya, S. Kundu, S. Zhong, J. Shim, E. Darian, O. Guvench, P. Lopes, I. Vorobyov, A. D. MacKerell, Jr., *J. Comput. Chem.* **2010**, *31*, 671 – 690; b) W. Humphrey, A. Dalke, K. Schulten, *J. Mol. Graph.* **1996**, *14*, 33 – 38.
[31] J. C. Phillips, R. Braun, W. Wang, J. Gumbart, E. Tajkhorshid, E. Villa, C. Chipot, R. D. Skeel, L. Kalé, K. Schulten, *J. Comput. Chem.* **2005**, *26*, 1781 – 1802.
[32] C. Crestini, F. Melone, M. Sette, R. Saladino, *Biomacromolecules* **2011**, *12*, 3928 – 3935.
[33] R. J. Millington, J. P. Quirk, *Trans. Faraday Soc.* **1961**, *57*, 1200 – 1207.
[34] G. L. Comstock, *Wood Fiber* **1970**, *1*, 283 – 289.
[35] P. Sannigrahi, D. H. Kim, S. Jung, A. Ragauskas, *Energy Environ. Sci.* **2011**, *4*, 1306 – 1310.
[36] B. S. Donohoe, S. R. Decker, M. P. Tucker, M. E. Himmel, T. B. Vinzant, *Biotechnol. Bioeng.* **2008**, *101*, 913 – 925.
[37] a) M. R. Sturgeon, S. Kim, K. Lawrence, R. S. Paton, S. C. Chmely, M. Nimlos, T. D. Foust, G. T. Beckham, *ACS Sustainable Chem. Eng.* **2014**, *2*, 472 – 485; b) K. Shimada, S. Hosoya, T. Ikeda, *J. Wood Chem. Technol.* **1997**, *17*, 57 – 72.
[38] B. Tjaden, S. J. Cooper, D. J. L. Brett, D. Kramer, P. R. Shearing, *Curr. Opin. Biotechnol.* **2016**, *12*, 44 – 51.
[39] a) D. W. Rutherford, R. L. Wershaw, L. G. Cox, U. S. Geological Survey, Reston, VA, **2004**; b) R. M. Kellogg, F. F. Wangaard, *Wood Fiber Sci.* **1969**, *1*, 180 – 204; c) *Wood Handbook: Wood as an Engineering Material* (Ed.: R. J. Ross), 2010 Edition ed., Forest Products Society, Madison, Wisconsin, USA, **2011**.
[40] a) G. F. Froment, K. B. Bischoff, *Chemical Reactor Analysis and Design, 2nd ed.*, Wiley, New York, NY, USA, **1990**, chap. 3; b) O. Levenspiel, *Chemical Reaction Engineering, 3rd ed.*, Wiley, New York, NY, USA, **1998**, chap. 18.
[41] R. Aris, *Chem. Eng. Sci.* **1957**, *6*, 262 – 268.
[42] H. Hartmann, T. Böhm, P. Daugbjerg Jensen, M. Temmerman, F. Rabier, M. Golser, *Biomass Bioenergy* **2006**, *30*, 944 – 953.
[43] a) I. W. McCahill, S. P. Hazen, *Trends Plant Sci.* **2019**, *24*, 853 – 866; b) F. Yang, P. Mitra, L. Zhang, L. Prak, Y. Verhertbruggen, J.-S. Kim, L. Sun, K. Zheng, K. Tang, M. Auer, H. V. Scheller, D. Loqué, *Plant Biotechnol. J.* **2013**, *11*, 325 – 335.
[44] V. S. P. Bitra, A. R. Womac, C. Igathinathane, P. I. Miu, Y. T. Yang, D. R. Smith, N. Chevanan, S. Sokhansanj, *Bioresour. Technol.* **2009**, *100*, 6578 – 6585.
[45] a) M. D. Smith, B. Mostofian, X. Cheng, L. Petridis, C. M. Cai, C. E. Wyman, J. C. Smith, *Green Chem.* **2016**, *18*, 1268 – 1277; b) L. Petridis, J. C. Smith, *ChemSusChem* **2016**, *9*, 289 – 295.
[46] a) C. Schuerch, *J. Am. Chem. Soc.* **1952**, *74*, 5061 – 5067; b) D. T. Balogh, A. A. S. Curvelo, R. A. M. C. De Groote, *Holzforschung* **1992**, *46*, 343 – 348.
[47] a) W. Schutyser, S. Van den Bosch, T. Renders, T. De Boe, S. F. Koelewijn, A. Dewaele, T. Ennaert, O. Verkinderen, B. Goderis, C. M. Courtin, B. F. Sels, *Green Chem.* **2015**, *17*, 5035 – 5045; b) T. Renders, S. Van den Bosch, T. Vangeel, T. Ennaert, S.-F. Koelewijn, G. Van den Bossche, C. M. Courtin, W. Schutyser, B. F. Sels, *ACS Sustainable Chem. Eng.* **2016**, *4*, 6894 – 6904.
[48] a) S. Li, K. Lundquist, U. Westermark, *Nord. Pulp Pap. Res. J.* **2000**, *15*, **2000**, 292; b) S. Omori, M. Aoyama, A. Sakakibara, *Holzforschung* **1998**, *52*, 391 – 397.
[49] I. Kumaniaev, J. S. M. Samec, *Ind. Eng. Chem. Res.* **2019**, *58*, 6899 – 6906.
[50] a) L. Shuai, M. T. Amiri, Y. M. Questell-Santiago, F. Héroguel, Y. Li, H. Kim, R. Meilan, C. Chapple, J. Ralph, J. S. Luterbacher, *Science* **2016**, *354*, 329 – 333; b) W. Lan, M. T. Amiri, C. M. Hunston, J. S. Luterbacher, *Angew. Chem. Int. Ed.* **2018**, *57*, 1356 – 1360; *Angew. Chem.* **2018**, *130*, 1370 – 1374; c) P. J. Deuss, M. Scott, F. Tran, N. J. Westwood, J. G. de Vries, K. Barta, *J. Am. Chem. Soc.* **2015**, *137*, 7456 – 7467.
[51] a) J. Yan, A. Aznar, C. Chalvin, D. S. Birdseye, E. E. K. Baidoo, A. Eudes, P. M. Shih, D. Loqué, A. Zhang, H. V. Scheller, *Biotechnol. Biofuels* **2018**, *11*, 195; b) C. Xu, X. Fu, R. Liu, L. Guo, L. Ran, C. Li, Q. Tian, B. Jiao, B. Wang, K. Luo, *Tree Physiol.* **2017**, *37*, 1713 – 1726.
[52] a) I. Porth, J. Klápště, O. Skyba, B. S. K. Lai, A. Geraldes, W. Muchero, G. A. Tuskan, C. J. Douglas, Y. A. El-Kassaby, S. D. Mansfield, *New Phytol.* **2013**, *197*, 777 – 790; b) P. Sannigrahi, A. J. Ragauskas, G. A. Tuskan, *Biofuels Bioprod. Biorefin.* **2010**, *4*, 209 – 226.
[53] a) M. H. Studer, J. D. DeMartini, M. F. Davis, R. W. Sykes, B. Davison, M. Keller, G. A. Tuskan, C. E. Wyman, *Proc. Natl. Acad. Sci. USA* **2011**, *108*, 6300 – 6305; b) S. Bhagia, W. Muchero, R. Kumar, G. A. Tuskan, C. E. Wyman, *Biotechnol. Biofuels* **2016**, *9*, 106.
[54] a) R. Franke, C. M. McMichael, K. Meyer, A. M. Shirley, J. C. Cusumano, C. Chapple, *Plant J.* **2000**, *22*, 223 – 234; b) H. Luo, M. M. Abu-Omar, *Green Chem.* **2018**, *20*, 745 – 753.
[55] a) P. Oyarce, B. De Meester, F. Fonseca, L. de Vries, G. Goeminne, A. Pallidis, R. De Rycke, Y. Tsuji, Y. Li, S. Van den Bosch, B. Sels, J. Ralph, R. Vanholme, W. Boerjan, *Nat. Plants* **2019**, *5*, 225 – 237; b) M. J. Orella, T. Z. H. Gani, J. V. Vermaas, M. L. Stone, E. M. Anderson, G. T. Beckham, F. R. Brushett, Y. Román-Leshkov, *ACS Sustainable Chem. Eng.* **2019**, *7*, 18313 – 18322.
[56] A. Eudes, A. George, P. Mukerjee, J. S. Kim, B. Pollet, P. I. Benke, F. Yang, P. Mitra, L. Sun, Ö. P. Çetinkol, S. Chabout, G. Mouille, L. Soubigou-Taconnat, S. Balzergue, S. Singh, B. M. Holmes, A. Mukhopadhyay, J. D. Keasling, B. A. Simmons, C. Lapierre, J. Ralph, D. Loqué, *Plant Biotechnol. J.* **2012**, *10*, 609 – 620.
[57] a) B. D. Mar, H. J. Kulik, *J. Phys. Chem. A* **2017**, *121*, 532 – 543; b) L. Berstis, T. Elder, M. Crowley, G. T. Beckham, *ACS Sustainable Chem. Eng.* **2016**, *4*, 5327 – 5335.
[58] Y. Mottiar, R. Vanholme, W. Boerjan, J. Ralph, S. D. Mansfield, *Curr. Opin. Biotechnol.* **2016**, *37*, 190 – 200.
[59] M. Harasek, B. Haddadi, C. Jordan, A. Friedl in *Computer Aided Chemical Engineering, Vol. 43* (Eds.: A. Friedl, J. J. Klemeš, S. Radl, P. S. Varbanov, T. Wallek), Elsevier, **2018**, pp. 1583 – 1588.
[60] a) C. G. Wilkerson, S. D. Mansfield, F. Lu, S. Withers, J.-Y. Park, S. D. Karlen, E. Gonzales-Vigil, D. Padmakshan, F. Unda, J. Rencoret, J. Ralph, *Science* **2014**, *344*, 90 – 93; b) W. Lan, F. Lu, M. Regner, Y. Zhu, J. Rencoret, S. A. Ralph, U. I. Zakai, K. Morreel, W. Boerjan, J. Ralph, *Plant Physiol.* **2015**, *167*, 1284 – 1295.
[61] J. Ralph, *Phytochem. Rev.* **2010**, *9*, 65 – 83.
[62] L. A. Donaldson, J. P. Knox, *Plant Physiol.* **2012**, *158*, 642 – 653.
[63] a) W. Muchero, J. Guo, S. P. DiFazio, J.-G. Chen, P. Ranjan, G. T. Slavov, L. E. Gunter, S. Jawdy, A. C. Bryan, R. Sykes, A. Ziebell, J. Klápště, I. Porth, O. Skyba, F. Unda, Y. A. El-Kassaby, C. J. Douglas, S. D. Mansfield, J. Martin, W. Schackwitz, L. M. Evans, O. Czarnecki, G. A. Tuskan, *BMC Genomics* **2015**, *16*, 24; b) B. S. F. Müller, J. E. de Almeida Filho, B. M. Lima, C. C. Garcia, A. Missiaggia, A. M. Aguiar, E. Takahashi, M. Kirst, S. A. Gezan, O. B. Silva-Junior, L. G. Neves, D. Grattapaglia, *New Phytol.* **2019**, *221*, 818 – 833; c) C. Riedelsheimer, J. Lisec, A. Czedik-Eysenberg, R. Sulpice, A. Flis, C. Grieder, T. Altmann, M. Stitt, L. Willmitzer, A. E. Melchinger, *Proc. Natl. Acad. Sci. USA* **2012**, *109*, 8872 – 8877; d) G. A. Tuskan, W. Muchero, T. J. Tschaplinski, A. J. Ragauskas, *Curr. Opin. Biotechnol.* **2019**, *56*, 250 – 257.

Manuscript received: March 1, 2020
Accepted manuscript online: April 3, 2020
Version of record online: May 8, 2020